

Synthesis and Characterizations of Metal Nanostructures for Application in Direct Alcohol Fuel Cells

Sahil Dahiya

M.Sc Student
Department of Chemistry
All India Jat Heros Memorial College, Rohtak.

Abstract:

This study reports the successful synthesis of Au@Pd bipyramidal core-shell nanoparticles with varying Pd shell thicknesses using a seed-mediated chemical growth method. The nanoparticles exhibit 5-fold twins with stacking faults, inducing tensile strain in the Pd shells, which decreases as shell thickness increases. Microstrain arising from defects further influences structural properties. The ultrathin Pd-shell nanoparticles demonstrate exceptional catalytic performance, achieving mass and specific activities 23.26 and 10 times higher than commercial Pd/C, respectively, along with superior durability in ethanol oxidation reactions (EOR). The findings highlight the importance of shell thickness tuning for designing highly efficient core-shell catalysts for fuel cell applications.

Keywords: Au@Pd, Pd-shell nanoparticles, TEM Images, HRTEM.

I. INTRODUCTION

Direct alcohol fuel cells are considered one of the promising and sustainable energy conversion devices potentially applicable to the power supply of vehicles and mobile electronics. DAFCs utilize the chemical energy of alcohol to generate electricity through alcohol oxidation reactions [1,2]. DAFCs are more advantageous and secure to be stored and transported compared to hydrogen fuel cells.

Among different types of alcohols, ethylene glycol (EG), ethanol, and glycerol have the advantage as fuel because these alcohols possess very high energy density with lower toxicity, and also, they are biorenewable and less volatile [3-6]. However, the electrooxidation conversion efficiency of these alcohols is usually inferior to hydrogen oxidation. This is because of the sluggish kinetics of electrooxidation of these alcohols, which is a multielectron transfer process [7-9].

Therefore, the design and synthesis of efficient electrocatalysts for the oxidation of these alcohols are highly desirable for the final commercialization of DAFCs.

In this regard noble metal and non-noble metal-based catalysts have been designed to boost AORs. Although, the lower onset potential of noble metal catalysts (Pd, Pt, and Rh) originated from their unique electronic structure makes them superior to non-noble metals (Ni, Co, and Mn) for the construction of high-performance DAFCs [10, 11]. To address the lack of noble metals, many attempts have been made to improve their catalytic activities by introducing the strain effect, electronic effect and ligand effect. Among all the above effects strain effect has proven to be more effective to boost the catalytic activity of noble metals. In the strained catalysts, metal-metal bond distance deviated from their intrinsic value, leading to a shift in the d-band center and a diverse electronic structure [12, 13]. The diverse electronic structure and shifted d-band center in the catalysts make a change in the adsorption ability of the catalytic active site towards reactant molecules and reaction intermediates [14]. Strained catalysts can be formed by constructing a core-shell structure, and the

amount of strain generated in the shell is governed by the degree of lattice mismatch between the core and shell [16, 18]. Strains can also be introduced in alloy nanoparticles and also in nanocrystals having crystal defects, such as twin boundaries. In the alloy nanoparticles, the strength of the strain in the surface of the nanoparticles depends on the size difference of the main atom from the doped atom. Along with the strain effect, catalytic property of the alloy also depends on the ligand effect, in which, coordinated atom of the metal site can tune the electronic structure and d-band center of the noble metals finely. Thus, the modification of the coordination atoms can offer a possible pathway to optimize the adsorption ability of the catalysts towards the reaction intermediates [19,20]. In twinned nanocrystals, twin boundaries can improve the catalytic property with the strain effect originated from the distortion of crystal structure near the twin boundaries. It can also directly enhance the catalytic property by functioning as the active site with high reactivity and adsorption ability towards the reactant and intermediate molecules.

In the context of strain engineering, Yang et al. employed epitaxial growth on gold nanorods to induce tensile strain in the palladium-platinum (PdPt) alloy shell [21]. Meanwhile, Liu et al. achieved a comparable outcome by epitaxially growing palladium (Pd) layers on silver nanoplates within the silver-palladium (AgPd) shell [22]. Han et al. introduced tensile strain within platinum (Pt) nanorings through a strategic doping process involving bismuth (Bi) atom. Furthermore, Liu et al. incorporated multiple twin boundaries into palladium (Pd) nanoparticles to induce the desired strain effect [23]. Although many endeavors have been made towards strain engineering of noble metal nanoparticles, it still remains a challenge to design catalysts with optimized electronic effects to boost the electrocatalytic activity towards AOR to even higher level.

Towards this direction, herein, we report a somewhat different approach to synthesize strain engineered Au@Pd core-shell NPs using a seed mediated chemical growth route for improved ethanol oxidation reactions. The core-shell structure here is implemented by forming the epitaxially grown Pd shell around an optimally size selected bipyramid (BP) shaped Au core. The advantage of using BP shaped metal core is to exploit the effect of its' structural defects such as 5-fold twins, micro twins, and stacking faults which in turn are expected to contribute to a part of the overall increment in the strain generated in the core-shell NP. Such a novel approach of generating core-shell structure has not been explored earlier. The present work demonstrates that Au@Pd core-shell NPs having the thinnest Pd shell shows the highest electrocatalytic activity towards ethanol oxidation compared to the NPs having thicker Pd shell and commercial Pd/C. More importantly, the synthesized Au@Pd core-shell nanostructures exhibit extraordinary high electrocatalytic activities up to the highest level of mass activity of 15.26 A mg⁻¹ Pd and specific activity of 13.69 mA cm⁻². These values are 23.26 and 10 times higher than that of the commercial Pd/C. The activity values observed here are higher than that of most of the Pd-based electrocatalysts reported to date in the literature [24].

II. SYNTHESIS OF NANOSTRUCTURES

2.2.1 Materials

Sodium tetrachloropalladate(II) (Na₂PdCl₄, 99%), ethylene glycol (EG), N,N dimethylformamide (DMF), polyvinylpyrrolidone (PVP, Mw ≈ 55000), Pd/C (10 wt.% Pd), silver nitrate (AgNO₃, extrapure, 99.5%), Gold (III) chloride trihydrate (HAuCl₄.3H₂O; ≥ 99.9% trace metals basis), L-ascorbic acid (AA, extrapure AR, 99.7%), sodium borohydride (NaBH₄, 98%), palladium chloride (PdCl₂, 99%), hexadecyl trimethylammonium bromide (CTAB, extrapure AR, 99%), were received from Sigma-Aldrich. Ethanol, Hydrochloric acid (HCl; 37%), citric acid, glycerol, potassium hydroxide (KOH, AR), and Copper chloride dihydrate (CuCl₂·2H₂O, ≥ 99%) were purchased from Merck. Hexadecyl trimethylammonium chloride (CTAC, 97%) was received from Alfa Aesar. The chemicals and reagents were used as received without undergoing further purification. Deionized water (DI water) with a resistivity of 18.2 MΩ.cm was used in all experiments and synthesis procedures. 0.1773 g PdCl₂ was added in 10 mL HCL (0.2 M) solution and it was further diluted to 100 mL with DI water to get 10 mM H₂PdCl₄.

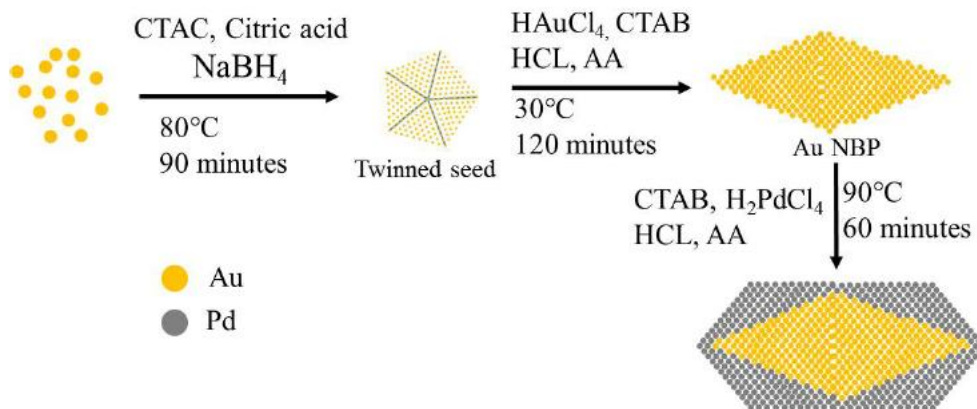


Figure 1: (a) A schematic presentation of synthesis of Au@Pd NP using seed mediated growth method.

We chose Au NBP as the core to prepare Au@Pd core-shell structures. To synthesize (Au NBP core)@(Pd shell) bimetallic NPs, we followed a seed-mediated growth method of preparing pentatwinned Au NBP seeds in the first stage and then deposited different amounts of Pd in the second stage on Au NBP seeds produced in the first stage

III. MORPHOLOGICAL, STRUCTURAL, AND COMPOSITIONAL ANALYSIS

As-synthesized and centrifuged Au NBP core and Au@Pd core-shell NPs were drop casted on carbon coated 300 mesh copper grids for TEM study. The morphology of the bipyramids has been obtained from the analysis of both bright field (BF) and high resolution (HR) TEM images. Bipyramids with large aspect ratios ($AR \geq 2.5$) are most often observed with the elongation direction parallel to the carbon grid, that is, perpendicular to the electron beam. They are always characterized by a nonuniform contrast and the presence of planar defects.

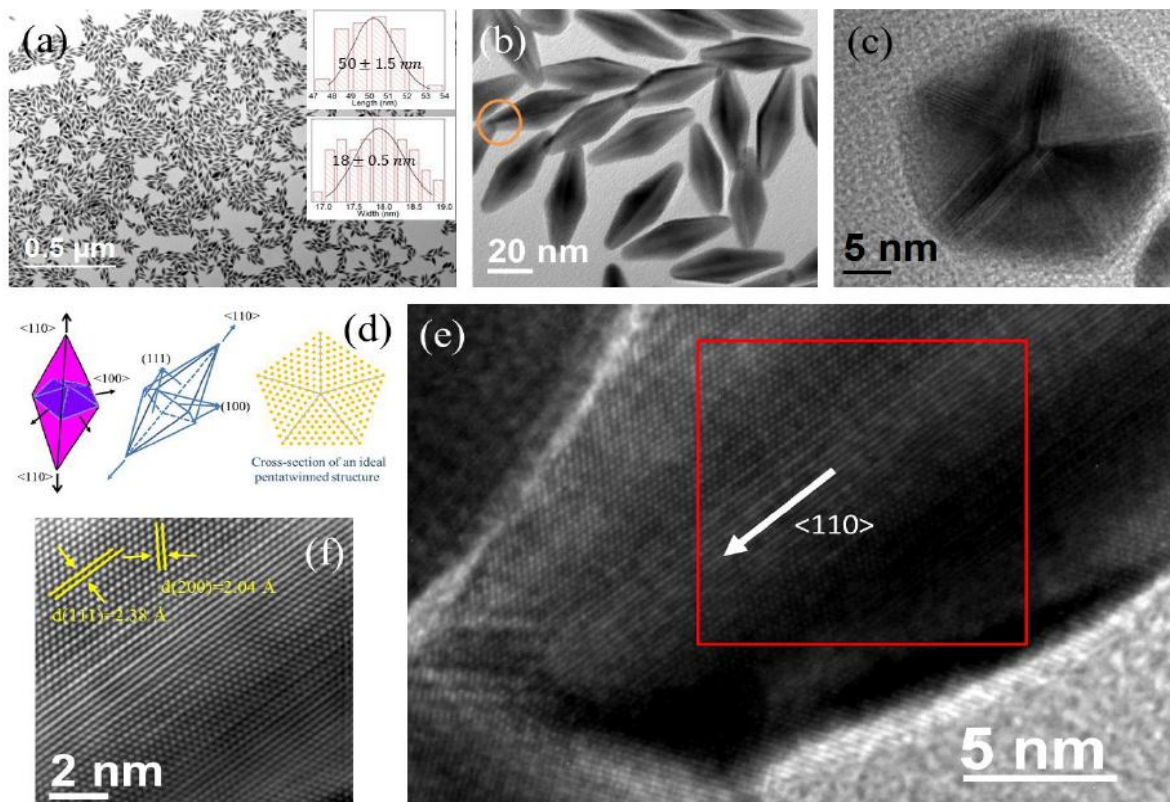


Figure 2: (a) and (b) are the TEM images of Au NBP NPs of length 50 nm at different magnifications. Inset: Average length and waist diameter. (c) HRTEM image of a pentatwinned Au nanoparticle grown in the growth solution for 20 min. (d) Schematic diagram of an Au BP and cross-section of an ideal pentatwinned structure. (e) HRTEM image of an Au NBP of length 50 nm. (f) Fourier filtered image of the selected area in (e).

From the analysis of several NPs, it appears that the large bipyramids are always twinned. Formation of almost monodisperse Au NBP seeds with the average length and waist diameter of 50 ± 1.5 nm and 18 ± 0.5 nm respectively was confirmed from the TEM image (Figure 2 a). For the sake of clarity, an enlarged view of a few isolated single NBPs selected randomly from the Figure 2 a is displayed in the high magnification TEM image of Figure 3.1b. The morphology (Figure 2b) of the as-synthesized Au bipyramids is characterized by a pentagonal base and two rounded apexes as distinguishable from the BF TEM image (Figure 3.1b). For different samples, the average apex angle formed between the extended side edge lines varies from 26 to 30°. The HRTEM image of an Au NP grown in the growth solution for 20 min is displayed in Figure 3.1c which clearly reveals that the pentatwinned nature of the as-synthesized Au NBP particles exhibiting a 5-fold symmetry. The schematic diagram of an ideal five-fold twinned Au NBP structure with a Penta twinned cross-section is depicted in Figure 3.1d. Five single crystalline segments share a common [10] axis and join together at {111} twinned planes cyclically. Each segment is exposing a {111} side surface parallel to the [10] twinning axis. The HRTEM analysis of an intermediate sized pentatwinned Au nanobipyramid (Figure 2c) and apex region of a full grown. Au NBP (Figure 2e) agrees well with the structural model depicted in Figure 2d except the presence of a large amount of stacking faults at the twin boundaries. Further, the different contrasts inside the twinning boundaries (Figure 2c) are due to the presence of microtwins and stacking faults. From the HRTEM image of Figure 2e, the lattice fringes within the Au subcrystals near the boundaries can be clearly recognized. The appearance of anomalous contrast fringes (Figure 2c and Figure 2e) in the Au subcrystals justify the presence of a high density of stacking faults in addition to the twinning boundaries observed here. The region slightly away from the stacking faults rich twin boundaries of the Au NBP along the $\langle 110 \rangle$ direction is characterized by the defect free single crystalline regions (SCRs) having continuous lattice fringes with lattice spacing 2.38 Å (Figure 3.1f) that could be assigned to the (111) plane of fcc Au. 5-fold twinned structures observed in the as-synthesized nanobipyramid shaped NPs being a common crystal defects are also found in the nanorod and nanowires of Au and other fcc metals [11].

The morphological evolution of Au@Pd NPs is shown in the BF TEM images Figure 3 a-c. HRTEM image confirms the successful preparation of the core-shell nanostructure (Figure 3 d). The shell thickness varies from waist to apex region of the bipyramid and the measured Pd shell thickness was the maximum near the apex region (about 3 nm) and the minimum at the waist (about 1 nm) for typical coreshell NP. Different molar ratios of Pd precursors lead to the formation of Au@Pd

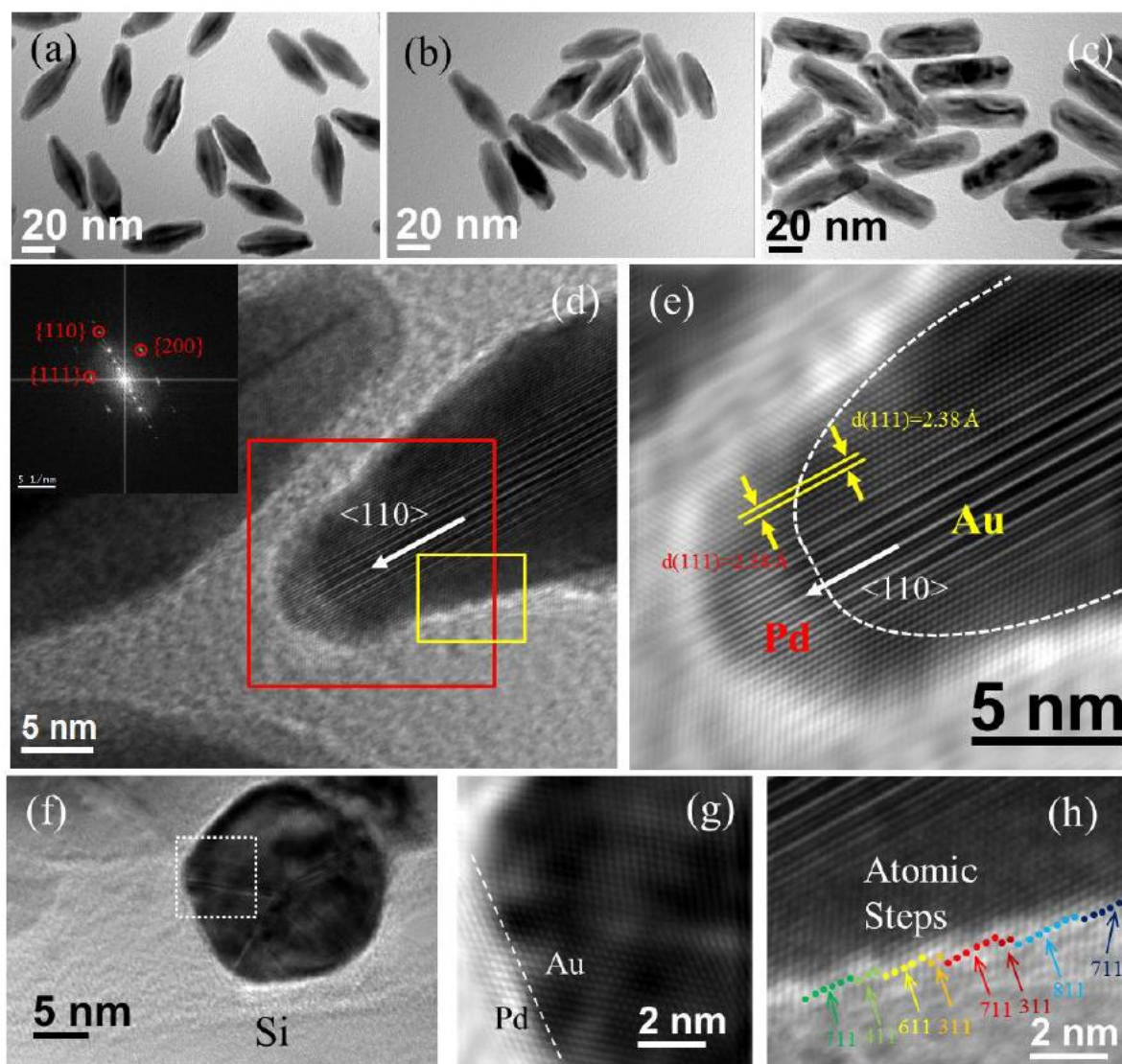


Figure 3: Bright-field TEM images of (a) Au@Pd 50-42 NPs, (b) Au@Pd 50-84 NPs, and (c) Au@Pd 50-168 NPs. (d) HRTEM image of an Au@Pd 50-42 core-shell NP with FFT pattern of the selected area with red square box in (d) in the inset. (e) Fourier filtered image of the selected area with red square box in (d). (f) Cross-sectional HRTEM image of an Au@Pd 50-84 core-shell. (g) Fourier filtered image of the selected area in (f). (h) Enlarged image of the selected yellow box in Fig. (d).

nanoparticles with different shell thicknesses and the outermost surface of Au@Pd NP morphology gradually turns from a bipyramid (BP) shape to a rod-like shape (Figure 3c) with the increase in Pd mole fraction. The notation “Au@Pd 50-42” indicates that the Pd shell was grown on an Au NBP core of length 50 nm using (42 μ L, 10 mM) H₂PdCl₄ solution. Consequently, Au@Pd 50-42, Au@Pd 50-84, and Au@Pd 50-168 mean the Au@Pd core-shell NPs with Pd shell thickness in the ascending order, and hereafter, we will use such notations quite often in the subsequent discussion of this paper. Due to the variation of Pd shell thickness over the side wall of a bipyramid core, we will mean the average shell thickness whenever we mention the Pd shell thickness of the Au@Pd core-shell NPs in this paper. Accordingly, the HRTEM image shown in Figure 3 d corresponding to the notation Au@Pd 50-42 indicates a core-shell particle with the lowest thickness of the Pd shell. To understand the atomic arrangements of the Pd shell on the Au NBP core, the Fourier filtered image of the red squared box region of Figure 3 d is displayed in Figure 3 e. The continuous lattice fringes from the Au core to the Pd shell are clearly discernible (Figure 3 e). The (111) lattice fringes with a spacing of 2.38 Å (lattice parameter of Au core) extended from the central region of the Au core to the Pd shell tip edge of the

NBP without variations in the d-spacing (inter planar distances) confirming the epitaxial growth of Pd shell on the Au core [12]. Consequently, the lattice size of the Pd shell of the core-shell NP is solely determined by the Au core and expands substantially from its intrinsic value (2.24 Å), generating intense tensile strain within the Pd shell. It has been reported that the conformal epitaxial growth of the Pd layer on the Au surfaces can occur when the layer growth rate is adequately low [18].

To check whether the cross-section of an elongated Au@Pd core-shell structure maintains the pentatwin nature, the Au@Pd core-shell NPs after the final stage of the synthesis step were drop casted and dried on Si substrate where the Au@Pd core-shell NPs are lying elongated positions, i.e., parallel to the Si substrates. One such substrate covered with core-shell particles with medium shell thickness (Au@Pd 50-84) was selected for cross-section sample preparation. The HRTEM image of the cross-section of a typical Au@Pd core-shell (Au@Pd 50-84) particle is displayed in Figure 3 f exhibiting the presence of pentatwins and associated crystallographic defects, like, stacking faults and microtwins as observed in bare Au core structure. From the Fourier filtered image (Figure 3 g) of the white boxed region of Figure 3 f, epitaxial growth of Pd on Au core (at the white marked boundary of Figure 3g) is quite evident. Moreover, the stacking faults type defects appearing in the form of fringes at 5 twin boundaries running parallel to $\langle 110 \rangle$ axis are common features of both the bare Au NBP core (Figure 3c, e) as well as Au@Pd core-shell NPs (Figure 3d, f). Further, the presence of SCRs with (111) planes at a distance slightly away from twin boundaries are also a common feature for bare Au NBP core and for the Pd coated Au@Pd core-shell structures corresponding to the minimum (Au@Pd 50-42, Figure 3 d, e) as well as medium shell thickness. As the catalytic activities of the Au@Pd core-shell NPs are highly correlated to their atomic arrangement and surface orientation, the outer most surface of the Pd shell was closely inspected using HRTEM. Figure 3 h shows a thin outer surface edge of the Pd shell selected from the yellow box region of the upper portion of the Au@Pd core-shell particle of Figure 3 d, expressing the lattice fringes comprising of the (111) planes. The surface edge is full of zigzag monoatomic steps with the high-index facets denoted by different colours using the microfacet notation developed by Somorjai et al. [18]. Surprisingly, except for the NPs with the lowest shell thickness (Au@Pd 50-42), we did not find the presence of such high energy faceted atomic steps at the outer surface edge of the thicker core-shell particles.

IV. ELECTROCHEMICAL ANALYSIS

We probed the electrocatalytic activities of the as-synthesized Au@Pd 50-42 NPs in EOR and compared with the other Au@Pd NPs synthesized by us and commercial Pd/C. The ECSAs of the all Pd-based electrocatalysts were calculated from the CVs recorded in 1 M KOH (Figure 4). In each CV a well-defined peak appeared during reverse scan between -0.2 to -0.6 V (vs Ag/AgCl) due to the reduction of PdO monolayer.

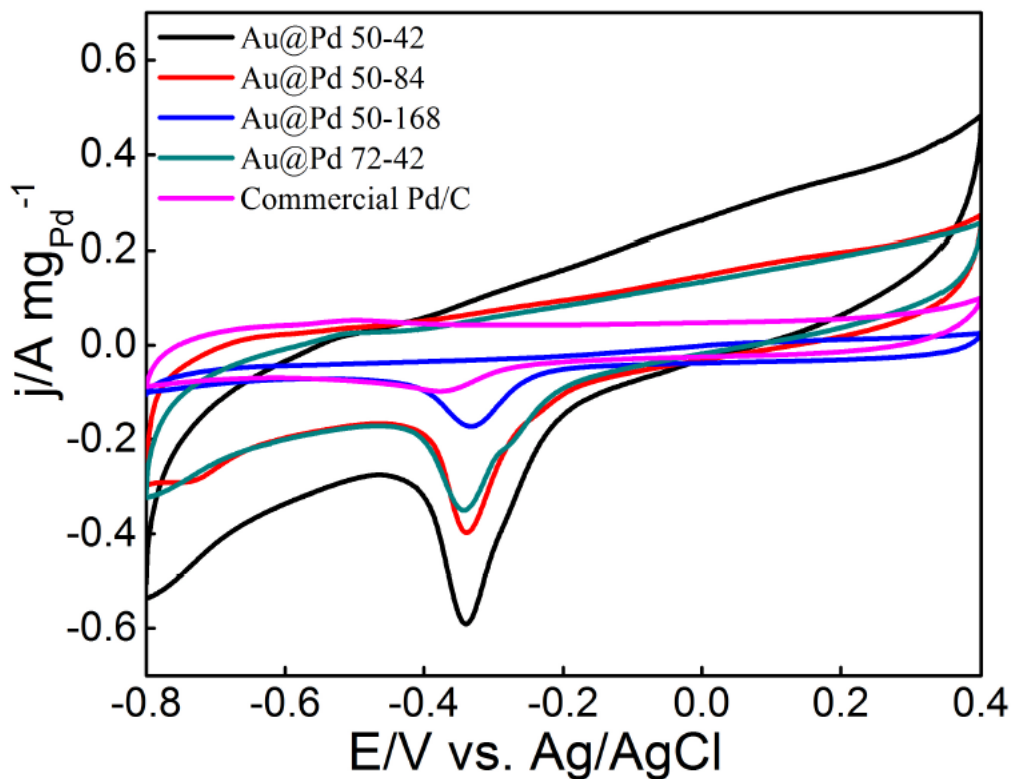


Figure 4: Cyclic voltammograms of the all Pd based catalysts recorded at room temperature in a solution containing 1 M KOH with a sweep rate of 50 mV/s.

The charge required for the reduction of PdO monolayer was calculated from the CVs by integrating the peaks and its surroundings. The electrochemically active surface areas (ECSAs) of the Pd based electrocatalysts were measured using the following formula.

$$ECSA = \frac{Q}{q \times W}$$

Where, q = Reference value for the reduction of PdO monolayer which is 4.05 C m^{-2} , Q is the charge required for the reduction of PdO monolayer and W is mass loading on the GC electrode. The value of Q can be determined from the CVs by integrating the reverse scan between -0.2 to -0.6 V (vs Ag/AgCl) and baseline. The calculated

ECSA values of the four Pd based catalysts are 111.5, 80.5, 73.6 and 47.9 m^2g^{-1} for Au@Pd 50-42, Au@Pd 50-84, and Au@Pd 50-168 core-shell NPs and commercial Pd/C, respectively (Figure 3.7). The mass activities and specific activities of the Au@Pd core-shell NPs with different shell thicknesses (Au@Pd 50-42, Au@Pd 50-84, and Au@Pd 50-168) with reference to a commercial Pd/C in EOR are displayed in Figure 5a and b.

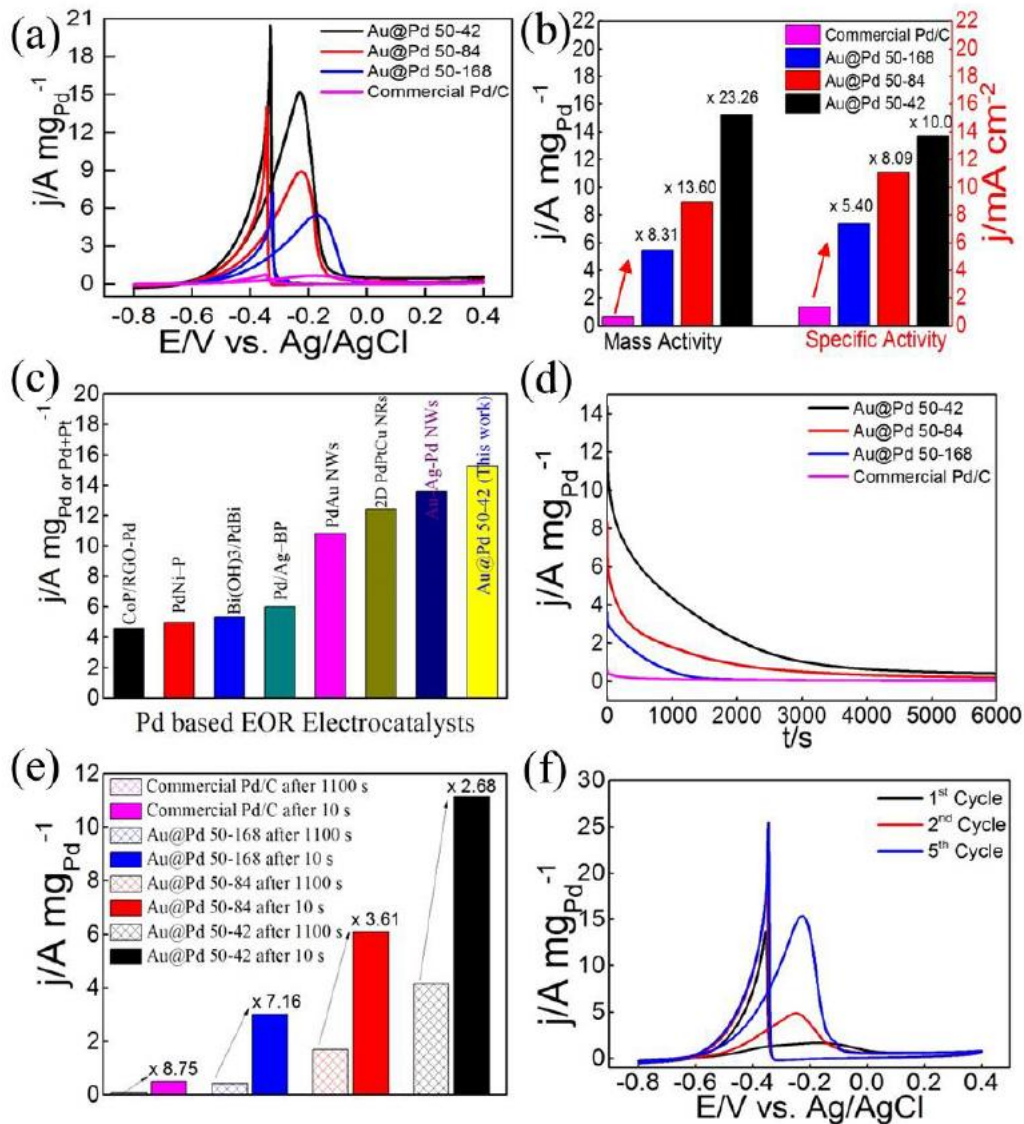


Figure 5: (a) Cyclic voltammograms of the four Pd-based catalysts recorded at room temperature in a solution containing 1 M ethanol and 1 M KOH with a sweep rate of 50 mV/s. (b) Histograms of mass and specific activities. (c) Comparison of EOR activity of Au@Pd 50-42 NPs with the Pd-based electrocatalyst's values reported previously [4]. (d) i-t curves of the four Pd-based catalysts were recorded at room temperature in a solution containing 1 M ethanol and 1 M KOH at -0.280 V versus Ag/AgCl. (e) Comparison of mass activities after 10 s and 1100 s of i-t test. (f) Cyclic voltammograms of the Au@Pd 50-42 NPs after i-t test.

The mass activities and specific activities of the catalysts are designated in terms of the anodic peak currents normalized to the mass of Pd loaded on the GC electrode and the ECSA, respectively. The CVs show that the onset potential of all the Au@Pd NPs is much lesser than the commercial Pd/C (about -0.445 V). Among all the catalysts, Au@Pd 50-42 NPs show the lowest onset potential (about -0.638 V) towards EOR, which indicates the acceleration in the ethanol oxidation reaction kinetics. In each CV, there are two peaks, the peak that appeared in the forward scan is due to the oxidation of ethanol and the peak that appeared in the backward scan is due to the oxidation and desorption of carbonaceous molecules [18]. We can see from the ethanol oxidation curve that with decreasing Pd shell thickness, the ethanol oxidation peak shifts to a more negative side which confirms a stronger absorption of ethanol and its intermediates.

As discussed in the previous sections of this paper, a thinner Pd shell offers stronger tensile strain and higher binding energy towards ethanol and its intermediates which further boosts the ethanol oxidation kinetics. It is also clear that EOR activities decrease with the increase in Pd shell thickness (Figure 5a). Also, the sharp edges, atomic steps, and tips of Au@Pd NPs could enhance the electrocatalytic activity [19, 20]. Among all the catalysts, core-shell NPs with the thinnest shell thickness employed here (Au@Pd 50-42) shows the highest mass activity (15.26 A mg⁻¹ Pd) which is about 1.71, 2.80, and 23.26 times higher than those of medium shell thickness (Au@Pd 50-84) (8.92 A mg⁻¹ Pd), and the highest shell thickness (Au@Pd 50-168) (5.45 A mg⁻¹ Pd) particles and commercial Pd/C (0.656 A mg⁻¹ Pd), respectively.

The core-shell NPs with the thinnest shell also exhibit the highest specific activity (13.69 mA cm⁻²) which is about 1.24, 1.85 and 10 times higher than those of medium shell thickness (11.08 mA cm⁻²), the highest shell thickness particles (7.4 mA cm⁻²), and commercial Pd/C (1.37 mA cm⁻²), respectively. The EOR activities (mass and specific activity) of the Au@Pd bipyramid core-shell structure with the thinnest shell (Au@Pd 50-42) employed in the present study substantially exceed those of most Pd based catalysts reported so far, making them a top ranked catalysts for this reaction to the best of our knowledge (Figure 5c).

Further to investigate the durability of the Au@Pd NPs and commercial Pd/C, chronoamperometric (i-t) curves were recorded in 1 M KOH and 1 M ethanol at constant potential of - 0.280 V (vs Ag/AgCl) for 6000 s (Figure 5d). The core-shell particles with the thinnest shell (Au@Pd 50-42 NP) show higher initial and final mass activity than the other Au@Pd NPs and commercial Pd/C. Due to the formation of PdO on the catalyst's surface mass activity of all the catalysts falls rapidly in the first 10 s. Commercial Pd/C showed almost no mass activity after EOR proceeded for 1100 s, while Au@Pd 50-42 NPs still showed 30% of their initial mass activity. Thus, Au@Pd core-shell nanobipyramids employed here also show enhanced catalytic durability compared with the commercial Pd/C under the same condition (Figure 5e). In real fuel cells, it is highly desirable that the electrocatalysts can clean their surface by an easy auto cleaning process for longer lifetime of the cells [58]. In this work, the partially deactivated Au@Pd 50-42 NPs can be reactivated by only sweeping five CV cycles in fresh 1 M KOH and 1 M ethanol (Figure 5f).

V. CONCLUSION

In summary, we have successfully synthesized Au@Pd bipyramid shaped core-shell nanoparticles with different Pd shell thicknesses using a seed mediated chemical growth route. The synthesized Au@Pd core-shell nanobipyramids possess 5-fold twins having parallel stacking faults at each of the 5 twin boundaries. The epitaxially grown Pd shells on the Au bipyramid core have the largest tensile strain for the Pd shell with the lowest thickness. The tensile strain generated in the Pd shell decreases with the increase in Pd shell thickness. Additionally, another type of crystallographic defects termed as “macrostrain” also exists in the core-shell structure induced by the presence of 5-fold twins, vacancies, and stacking faults at the twin boundaries. The Au@Pd NPs having the thinnest Pd shell employed here achieve extraordinary high mass and specific activities towards EOR which is 23.26 and 10 times higher, respectively than that of the commercial Pd/C. The core-shell nanoparticles with the ultrathin shell also exhibits the highest durability towards EOR in comparison to the other Pd-based electrocatalysts. The core-shell particles with the thicker Pd shell do also exhibit substantially higher activity in EOR as compared to the Pd/C. The present study indicates that tuning the thickness of the deposited catalytic metal layer over a noble metal core with a judiciously selected morphology may provide a guideline for constructing optimally strained core-shell structures for achieving highly efficient catalysts for ethanol as well as other alcohol-based fuel cells and associated applications.

REFERENCES:

1. Ibrahim Khan, Khalid Saeed, and Idrees Khan. “Nanoparticles: Properties, applications and toxicities”. In: Arabian journal of chemistry 12.7 (2019), pp. 908–931.

2. Yanli Wang et al. “Silicon nanowires for biosensing, energy storage, and conversion”. In: *Advanced materials* 25.37 (2013), pp. 5177–5195.
3. Philippe Sciau. *Nanoparticles in ancient materials: the metallic lustre decorations of medieval ceramics*. Vol. 115. INTECH Open Access Publisher, 2012.
4. William J Clinton. “Weekly compilation of presidential documents”. In: Washington, DC: Office (1999).
5. Ambler Thompson and Barry N Taylor. *Guide for the Use of the International System of Units (SI)*. Tech. rep. 2008.
6. RW Siegel. “Nanophase materials: synthesis, structure, and properties”. In: *Physics of new materials*. Springer, 1994, pp. 65–105.
7. Ye Chen et al. “Two–dimensional metal nanomaterials: synthesis, properties, and applications”. In: *Chemical reviews* 118.13 (2018), pp. 6409–6455.
8. Huanyu Jin et al. “Emerging two-dimensional nanomaterials for electrocatalysis”. In: *Chemical reviews* 118.13 (2018), pp. 6337–6408.
9. GK Thomas. “Tuning functional properties: From nanoscale building blocks to hybrid nanomaterials”. In: *Platin. Jubil. Spec. Publ* (2010), pp. 53–66.
10. Elena Degoli and Stefano Ossicini. “Engineering quantum confined silicon nanostructures: Ab–initio study of the structural, electronic and optical properties”. In: *Advances in Quantum Chemistry* 58 (2009), pp. 203–279.
11. Nicola Armaroli and Vincenzo Balzani. “The future of energy supply: challenges and opportunities”. In: *Angewandte Chemie International Edition* 46.1– 2 (2007), pp. 52–66.
12. VV Tyagi et al. “Progress in solar PV technology: Research and achievement”. In: *Renewable and sustainable energy reviews* 20 (2013), pp. 443–461.
13. Arian Bahrami et al. “Technical and economic analysis of wind energy potential in Uzbekistan”. In: *Journal of cleaner production* 223 (2019), pp. 801– 814.
14. Nick Watts et al. “Health and climate change: policy responses to protect public health”. In: *The lancet* 386.10006 (2015), pp. 1861–1914.
15. Frederica P Perera. “Multiple threats to child health from fossil fuel combustion: impacts of air pollution and climate change”. In: *Environmental health perspectives* 125.2 (2017), pp. 141–148.
16. Raman Ganesan and Jae Sung Lee. “Tungsten carbide microspheres as a noble–metal–economic electrocatalyst for methanol oxidation”. In: *Angewandte Chemie International Edition* 44.40 (2005), pp. 6557–6560.
17. Zhelin Liu et al. “Carbon nanotube/raspberry hollow Pd nanosphere hybrids for methanol, ethanol, and formic acid electro–oxidation in alkaline media”. In: *Journal of colloid and interface science* 351.1 (2010), pp. 233–238.
18. Bo You et al. “Enhancing electrocatalytic water splitting by strain engineering”. In: *Advanced Materials* 31.17 (2019), p. 1807001.
19. Shuangyin Wang and San Ping Jiang. “Prospects of fuel cell technologies”. In: *National Science Review* 4.2 (2017), pp. 163–166.
20. Xiaoyang Cui, Cheng Tang, and Qiang Zhang. “A review of electrocatalytic reduction of dinitrogen to ammonia under ambient conditions”. In: *Advanced Energy Materials* 8.22 (2018), p. 1800369.
21. Cheonghee Kim et al. “Alloy nanocatalysts for the electrochemical oxygen reduction (ORR) and the direct electrochemical carbon dioxide reduction reaction (CO₂RR)”. In: *Advanced materials* 31.31 (2019), p. 1805617.
22. Yingjie Li et al. “Recent advances on water–splitting electrocatalysis mediated by noble–metal–based nanostructured materials”. In: *Advanced Energy Materials* 10.11 (2020), p. 1903120.
23. Yuchao Wang et al. “Single atom catalysts for fuel cells and rechargeable batteries: principles, advances, and opportunities”. In: *ACS nano* 15.1 (2021), pp. 210–239. [24] Wei Wang et al. “Tuning

- nanowires and nanotubes for efficient fuel–cell electrocatalysis”. In: *Advanced Materials* 28.46 (2016), pp. 10117–10141.
24. Lin Huang et al. “Synergy between plasmonic and electrocatalytic activation of methanol oxidation on palladium–silver alloy nanotubes”. In: *Angewandte Chemie International Edition* 58.26 (2019), pp. 8794–8798.
25. Amare Aregahegn Dubale et al. “High–performance bismuth–doped nickel aerogel electrocatalyst for the methanol oxidation reaction”. In: *Angewandte Chemie International Edition* 59.33 (2020), pp. 13891–13899.
26. Chang Liu et al. “Air–assisted transient synthesis of metastable nickel oxide boosting alkaline fuel oxidation reaction”. In: *Advanced Energy Materials* 10.46 (2020), p. 2001397.
27. Ligang Chen et al. “Promoting electrocatalytic methanol oxidation of platinum nanoparticles by cerium modification”. In: *Nano Energy* 73 (2020), p. 104784.